



Wurster fluidised-bed coating: Coarse-graining technique within CFD-DEM in conjunction with heat and mass transfer

Downloaded from: <https://research.chalmers.se>, 2026-04-18 20:39 UTC

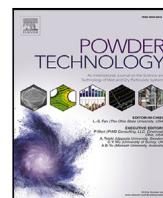
Citation for the original published paper (version of record):

Kjaer Jepsen, P., De Juan, L., Boje, A. et al (2024). Wurster fluidised-bed coating: Coarse-graining technique within CFD-DEM in conjunction with heat and mass transfer. *Powder Technology*, 443. <http://dx.doi.org/10.1016/j.powtec.2024.119901>

N.B. When citing this work, cite the original published paper.

Contents lists available at [ScienceDirect](https://www.sciencedirect.com)

Powder Technology

journal homepage: www.journals.elsevier.com/powder-technology

Wurster fluidised-bed coating: Coarse-graining technique within CFD-DEM in conjunction with heat and mass transfer

Philip Kjaer Jepsen^{a,*}, Luis Martin De Juan^b, Astrid Boje^c, Sohan Sarangi^b, Christian von Corswant^b, Srdjan Sasic^a

^a Department of Mechanics and Maritime Sciences, Chalmers University of Technology, Gothenburg, Sweden

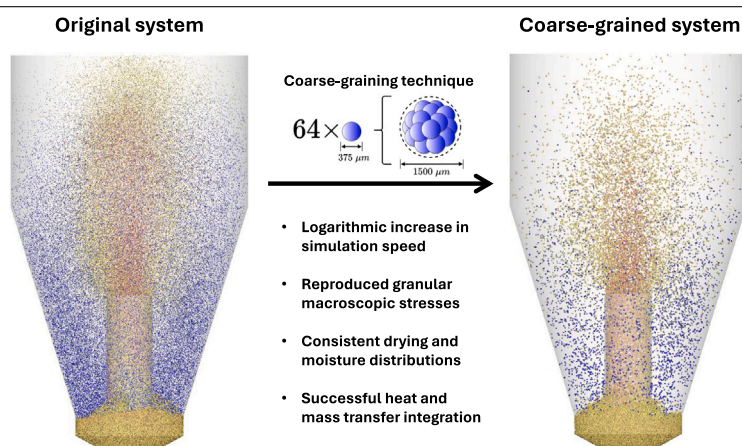
^b Oral Product Development, Pharmaceutical Technology & Development, AstraZeneca, Gothenburg, Sweden

^c Sustainable Innovation & Transformational Excellence, Pharmaceutical Technology & Development, AstraZeneca, Gothenburg, Sweden

HIGHLIGHTS

- Logarithmic simulation speed-up in CFD-DEM via coarse-graining (particle scaling).
- Modelling of solid, gas, and liquid phases in the Wurster fluidised-bed coating process.
- Evaluation of granular flow rheology, with analysis of inter-phase momentum, heat, and mass transfer.
- Experimental validation of CFD-DEM predictions with PEPT data.

GRAPHICAL ABSTRACT



ARTICLE INFO

Keywords:

CFD-DEM
Coarse-graining technique
Wurster fluidised-bed coater
Granular flow regime characterisation
Three-phase system
Liquid spray modelling

ABSTRACT

In this study, we use a combined CFD-Discrete Element Method to assess predictive capabilities and numerical implications of a coarse-graining technique in Wurster fluidised-bed coaters. We investigated both hydrodynamics and heat and mass transfer and conducted simulations of a full three-phase system for the original and three coarse-grained systems, analysing velocity distributions, macroscopic solid stresses, moisture content and phase temperatures. We achieved a logarithmic simulation speed-up by aggregating up to 64 original particles into each coarse grain. This was accomplished while maintaining fidelity to the original CFD-DEM system in terms of reproducing with high accuracy macroscopic granular flow properties in different regions of a coater (drying, tube and bed regions). By integrating a liquid spray and humid air, we demonstrated that the phase temperatures were accurately predicted within the coarse-grained system, with a high capability of delivering liquid spray distributions with the same uniformity and drying. We also give arguments for choosing a certain degree of coarse-graining as a compromise between a desired reduction of computational costs and a trustworthy reproduction of granular-flow physics encountered in different regions of a Wurster bed. Our findings pave the way to using CFD-DEM to industrially-scaled Wurster-bed systems, which is currently unfeasible due to prohibitive computational costs.

* Corresponding author.

E-mail address: jepsen@chalmers.se (P. Kjaer Jepsen).

<https://doi.org/10.1016/j.powtec.2024.119901>

Received 8 March 2024; Received in revised form 8 May 2024; Accepted 19 May 2024

Available online 21 May 2024

0032-5910/© 2024 The Author(s). Published by Elsevier B.V. This is an open access article under the CC BY license (<http://creativecommons.org/licenses/by/4.0/>).

Nomenclature

Abbreviations

CFD	Computational fluid dynamics
CT	Cycle time
DEM	Discrete element method
MCC	Microcrystalline cellulose
PCM	Particle centroid method
PEPT	Positron emission particle tracking
RT	Residence time
UDFs	User-Defined Functions

Greek symbols

α	Voidage, –
ω_i	Angular velocity, s^{-1}
τ	Shear stress tensor, $N\ m^{-2}$
δ	Relative displacement, m
$\dot{\gamma}_s$	Solids shear strain tensor, –
η_n	Damping coefficient, $\sqrt{kg\ Pa\ m}$
γ	Damping ratio, –
λ	Thermal conductivity, $W\ m^{-1}\ K^{-1}$
μ	Fluid viscosity, Pa s
μ_s	Particle friction coefficient, –
ν	Poisson ratio, –
ϕ	Relative humidity, –
ψ	Scaling factor, –
ρ	Density, $kg\ m^{-3}$
ϵ	Coefficient of restitution, –

Latin symbols

\hat{n}_{ij}	Normal unit vector, –
\hat{t}_{ij}	Tangential unit vector, –
F_i	Force, N
g	Gravity, $m\ s^{-2}$
u_i	Particle velocity, $m\ s^{-1}$
v	Gas velocity, $m\ s^{-1}$
x_i	Particle position, m
A	Area, m^2
C_d	Drag coefficient, –

c_p	Specific heat capacity, $J\ kg^{-1}\ K^{-1}$
D	Diffusion coefficient, $m^2\ s^{-1}$
d	Diameter, m
E	Young's modulus, Pa
H	Enthalpy, J
h	Heat transfer coefficient, $W\ m^{-2}\ K^{-1}$
h_c	Mass transfer coefficient, $m\ s^{-1}$
I	Inertial number, –
I_i	Moment of inertia, $kg\ m^2$
k_n	Hertz stiffness coefficient, Pa m
l	Branch vector, m
M	Molar mass, $g\ mol^{-1}$
m	Mass, kg
Nu	Nusselt number, –
p	Pressure, Pa
Q_i	Heat transfer, J
R	Radius, m
R_a	Universal gas constant, $J\ K^{-1}\ mol^{-1}$
Re	Reynolds number, –
Sh	Sherwood number, –
T	Temperature, K
t	Time, s
V	Volume, m^3
X_v	Moisture content, –
Y_v	Vapour mass fraction, –

Sub/superscripts

'	Effective
c	Computational cell
cg	Coarse grain
i, j	Particle index
l	Liquid
n, t	Normal, tangential component
o	Original (unscaled) particle
s	Solid
v	Vapour

1. Introduction

Fluidised-bed spray coating of particles, pellets or granules is ubiquitous in industries such as pharmaceuticals, chemicals, and food production, addressing functional objectives like modified release, sensory attribute masking, and shelf life extension [1]. The Wurster coater, a notable variant within fluidised-bed coaters due to its distinctive airflow and geometry, is acknowledged for its efficacy in producing high-quality films with minimal defects [2,3]. Illustrated in Fig. 1, pellets in the Wurster coater follow cyclical trajectories via three distinct regions. The fluidising gas enters the system through a distributor plate, featuring orifices with a higher open area in its annular region beneath the Wurster tube. This region surrounds the two-fluid nozzle, from which atomising air disperses the coating solution into a fine spray of liquid droplets. Consequently, the Venturi effect conveys pellets from the bed into the tube region for spraying. Upon entering the subsequent drying region, where rapid solvent evaporation occurs, the process of coating film formation on the pellets ensues [4,5].

To capitalise on the benefits of this technology, design, optimisation and risk mitigation are crucial, addressing challenges like film degradation and particle agglomeration [6]. Laboratory-scale Wurster coaters

equipped with advanced monitoring systems have been utilised to examine process variables and geometric influences [2,7,8]. However, challenges in particle enumeration and spatial resolution, along with the elevated costs and complexity for equivalent data accuracy, limit their extension to industrial-scale systems [9,10].

In the preceding decade, advancements in computational capabilities have expanded the utility of predictive modelling for multiphase gas-solid systems, common in industrial applications [11,12]. Two main numerical frameworks are commonly known as Euler–Euler [13, 14], which conceptualises the present phases as interpenetrating continua, and Euler–Lagrange, a part of which is known as CFD-DEM, where particles are tracked individually as discrete elements in a Lagrangian reference system and the fluidising gas is represented as a field [15,16]. In the Euler–Euler framework, the solid phase is often modelled via the kinetic theory of granular flow, assuming instantaneous collisions and, originally, uncorrelated velocities (molecular chaos) [17]. Conversely, CFD-DEM simulates particle interactions as deformable or non-deformable elements, capable of accommodating multiple sustained or binary instantaneous contacts, respectively [18].

Selecting an appropriate numerical framework includes comprehension of the intrinsic model assumptions, affordable computational

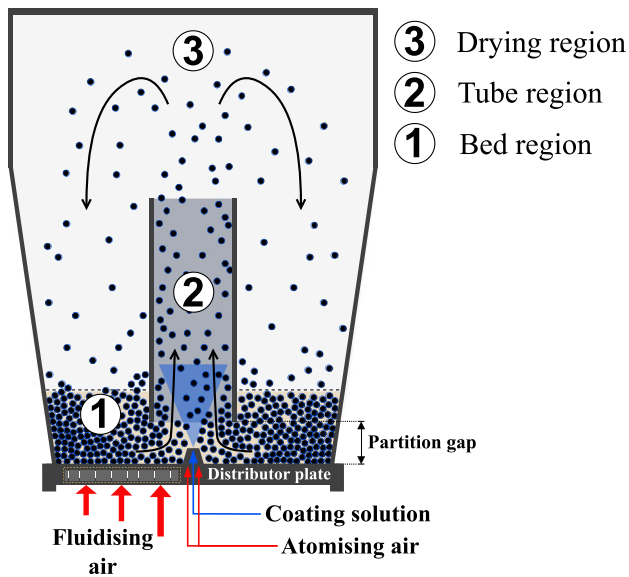


Fig. 1. Schematic depiction of characteristic regions within Wurster coaters: (1) the bed region, wherein particles are fluidised and horizontally conveyed, propelled by the Venturi effect into (2) the tube region, wherein particles are sprayed; followed by (3) the drying region, wherein the film coating process proceeds.

cost and their pertinence across distinct granular flow regimes. The observed behaviour varies significantly within these regimes, characterised by the complex ability of particles to behave collectively in manners reminiscent of solids, liquids or gases, dependent on the extent of packing and agitation [19]. In Wurster coaters, the solid concentration and agitation vary significantly, resulting from gas velocity differences within the annular region. Consequently, distinct flow regimes exist in the various sections of this geometry. In very dense regions, where particles undergo slow shear and frictional stresses arise from prolonged and multiple contacts, a quasi-static flow regime is discernible [20,21]. The inertial regime, characterised by increased particle inertia (strong agitation), leads to erratic motion predominantly governed by collisional stresses. However, the extent of frictional interactions in this regime is dependent on solid concentration: in a dilute inertial regime, collisional rapid flow exhibits gas-like characteristics, whereas, in a dense inertial regime, it transitions to a liquid-like flow where frictional contacts are influential [22–24].

The utility of CFD-DEM in various fluidised-bed systems, including Wurster coaters, is well-established [4,25–28]. While the computational demands of tracking individual particles primarily limit the application of CFD-DEM to laboratory-scale systems, advancements in parallel computing and DEM algorithms have broadened its applicability, facilitating simulations in fluidised-bed systems of up to 25 million particles [12,29]. Nonetheless, for industrial processes dealing with billions of particles, the computational costs remain prohibitively high. In response, several strategies have been developed, with coarse-graining (particle scaling) techniques receiving increasing attention in recent years. Practically, this involves aggregating particles into coarser grains while preserving their physical behaviour [30–32].

Early DEM scaling efforts primarily focused on hydrodynamic force scaling within fluidised beds, where these forces predominate [33]. In the past decade, the focus has shifted to include the precise scaling of contact forces for preserving complex characteristics, such as solid stresses and dissipative properties, which are crucial for describing the physics in dense regions [30]. According to the classification presented in [34], two principal types of coarse-graining methods are discerned: (1) direct force scaling by using similarity laws, which involves proportionally adjusting the forces on coarse grains to align with those on their original counterparts [33,35]; and (2) parameter scaling, where

the adjustment of contact forces is governed by the selected contact model and the scaling laws derived from dimensional analysis [36–40].

When it comes to Wurster coating systems, there is a relatively limited number of studies related to formulating and validating scaling techniques, and in them hydrodynamic force scaling has typically been used [41–43], with a recent exception where direct force scaling was utilised [44]. In the present study we thus have two goals: (i) to carry out a thorough numerical analysis of coupled hydrodynamic and heat-and-mass-transfer phenomena in Wurster beds in systems containing both the original number of particles and those with different levels of coarse-graining and (ii) to investigate the implications of employing parameter scaling on reproducing fundamental features of granular-flow physics encountered in different regions of a Wurster bed.

2. Methodology

2.1. Continuous-phase modelling

Starting with the volume-averaged equations for the conservation of mass and momentum in the gas phase [45]:

$$\frac{\partial}{\partial t}(\alpha\rho) + \nabla \cdot (\alpha\rho\mathbf{v}) = S_v, \quad (1)$$

$$\frac{\partial}{\partial t}(\alpha\rho\mathbf{v}) + \nabla \cdot (\alpha\rho\mathbf{v}\mathbf{v}) = -\alpha\nabla p + \nabla \cdot (\alpha\boldsymbol{\tau}) + \alpha\rho\mathbf{g} + \mathcal{S}. \quad (2)$$

Within the specified equations, α , ρ , and \mathbf{v} denote the voidage, density, and velocity of the gas, respectively. The source terms S_v and \mathcal{S} denote the volumetric inter-phase mass and momentum exchange between solids and gas. For the shear stress tensor, defined by $\boldsymbol{\tau} = \mu'(\nabla\mathbf{v} + \nabla\mathbf{v}^T - \frac{2}{3}\nabla \cdot \mathbf{v}\mathbf{I})$, where \mathbf{I} is the identity matrix and μ' is the effective viscosity, determined from the realisable $k-\epsilon$ turbulence model. The realisable version extends the standard $k-\epsilon$ model by introducing corrections to mitigate its tendency to overestimate turbulent viscosity and excessive dissipation, culminating in improved jet spreading [46].

The presence of humidity in the gas phase necessitates concurrently solving the energy conservation equation for the gas with an additional mass conservation equation for water vapour [47,48]:

$$\frac{\partial}{\partial t}(\alpha\rho c_p T) + \nabla \cdot (\alpha\rho c_p T\mathbf{v}) = \nabla \cdot (\alpha\lambda\nabla T + \rho D'_v \nabla Y_v H_v) + S_h, \quad (3)$$

$$\frac{\partial}{\partial t}(\alpha\rho Y_v) + \nabla \cdot (\alpha\rho Y_v\mathbf{v}) = \nabla \cdot (\alpha\rho D'_v \nabla Y_v) + S_v. \quad (4)$$

Here, c_p signifies the specific heat capacity, T the temperature, λ the thermal conductivity, and D'_v the effective mass diffusivity of the gas. Furthermore, Y_v denotes the vapour mass fraction, and H_v is the enthalpy of the vapour in the gas. The term S_h is defined as the convective heat transfer between the solids and the gas.

The computation of the inter-phase coupling terms will be presented in Section 2.2, whilst Section 2.3 details the liquid spray modelling approach, wherein solids are spray-coated with pure solvent water. Notably, Eq. (4) does not incorporate individual droplet tracking, precluding Eq. (3) from accounting for cooling effects due to droplet evaporation in the gas or spray. However, the exclusive incorporation of latent heat on the solids side will result in the evaporation from solids indirectly cooling the gas through the convective inter-phase coupling [47]. Additionally, we disregard the mass source term, S_v , in Eq. (1) related to solvent evaporation, owing to the negligible mass change in the gas phase attributed to this process.

2.2. Inter-phase coupling

The gas-phase Eqs. (1) to (4) are coupled to the solid phase within each computational cell V_c , by the presence of P particles, by the voidage and source terms \mathcal{S} and S_h . Voidage is computed via the particle centroid method (PCM), as $\alpha_c = 1 - \sum_{i=1}^P V_i/V_c$, based on particles with centroids in the cell. Nevertheless, PCM's ability to conserve quantities is compromised in highly dense systems or when $V_i \sim V_c$ [49]. To address this, we employ a diffusion-based coupling

method when $\alpha_c < 0.4$, implementing a diffusion equation of the form $\dot{\alpha}_c = -D\nabla^2\alpha_c$ across all domain cells. Initially computed using PCM cell values, this equation is iteratively solved while enforcing a no-flux boundary condition until $\alpha_c \geq 0.4$ [50,51]. We further refer to Appendix A for details regarding the numerical implementation.

The momentum exchange term, S , is derived from the hydrodynamic forces, $F_{f,i}$, acting upon each particle, as outlined in Eq. (5). Considering $\rho_i \gg \rho$ and pronounced pressure gradients – particularly in the vicinity of the nozzle – it is assumed that forces apart from drag and fluid pressure contribute insignificantly to particle dynamics, hence their exclusion [52]:

$$S = -\frac{1}{V_c} \sum_{i=1}^P F_{f,i} = \frac{1}{V_c} \sum_{i=1}^P \left[V_i \nabla p - \frac{1}{2} \rho A_i C_d |\mathbf{v} - \mathbf{u}_i| (\mathbf{v} - \mathbf{u}_i) \right]. \quad (5)$$

In Eq. (5), V_i , A_i and \mathbf{u}_i represent the particle volume, projected area and velocity, respectively. The selection of the Gidaspow drag model to compute $C_d = f(\alpha, Re_i)$ is based on a comparative analysis by Li et al. [25], which assessed various drag models within the Wurster coater system. The source term corresponding to convective inter-phase heat exchange, denoted by S_h in Eq. (3), is evaluated as [47]:

$$S_h = -\frac{1}{V_c} \sum_{i=1}^P Q_{f,i} = \frac{1}{V_c} \sum_{i=1}^P h A_i (T_i - T). \quad (6)$$

In this context, $Q_{f,i}$ is the convective heat flux from the i th particle, where A_i and T_i denote the surface area and temperature of the particle, respectively, whilst h signifies the convective heat transfer coefficient. Furthermore, S_v , in Eq. (3), quantifies the inter-phase mass transfer due to evaporation of the solvent from particles, and is expressed as follows:

$$S_v = \frac{1}{V_c} \sum_{i=1}^P \dot{m}_{v,i} = \frac{1}{V_c} \sum_{i=1}^P \frac{h_c A_i M_v}{R_a} \left[\frac{p_{v,i}}{T_i} - \frac{\phi p_v}{T} \right], \quad (7)$$

where $\dot{m}_{v,i}$ denotes the mass evaporation rate from the i th particle, the parameters h_c , M_j , R_a , and ϕ represent, respectively, the mass-transfer coefficient, the molar mass of water, the universal gas constant, and the local relative humidity. In Eq. (7), the vapour pressures at the particle surface and in the bulk phase are determined by applying the ideal gas law, assuming saturation at the particle surface to calculate $p_{v,i}$ using the Antoine equation. Heat and mass transfer coefficients in Eqs. (6) and (7) are derived using Sherwood and Nusselt numbers, $Sh = h_c d_i / D_v$ and $Nu = h d_i / \lambda$, respectively, employing Gunn's correlation for packed and fluidised beds [53].

2.3. Discrete-phase modelling

In the Lagrangian framework, the translational and angular velocities of the i th particle, denoted as \mathbf{u}_i and $\boldsymbol{\omega}_i$ and possessing a mass m_i and moment of inertia I_i , are ascertained through the following governing equations:

$$m_i \frac{d\mathbf{u}_i}{dt} = m_i \mathbf{g} + \mathbf{F}_{f,i} + \sum_{j=1}^J (\mathbf{F}_{n,ij} + \mathbf{F}_{t,ij}), \quad (8)$$

$$I_i \frac{d\boldsymbol{\omega}_i}{dt} = \sum_{j=1}^J R_i \hat{\mathbf{n}}_{ij} \times \mathbf{F}_{t,ij}, \quad (9)$$

where, in addition to the previously mentioned hydrodynamic forces, $\mathbf{F}_{n,ij}$ and $\mathbf{F}_{t,ij}$ denote the normal and tangential contact forces, respectively, emerging from interactions with J other particles or boundaries, conforming to a soft-sphere formulation, indicated by the overlap, which for two particles occurs when $\delta_n = d_i - (\mathbf{x}_i - \mathbf{x}_j) \cdot \hat{\mathbf{n}}_{ij} > 0$, with the normal unit vector $\hat{\mathbf{n}}_{ij} = (\mathbf{x}_i - \mathbf{x}_j) / |\mathbf{x}_i - \mathbf{x}_j|$ [15]. As seen from Eq. (9), the rotational motion is produced by collisions, as the generated torques are proportionally related to the tangential contact force. The normal force is defined per Hertz theory, augmented by Tsuji et al.'s viscous modifications while for the tangential component, the Mindlin-Deresiewicz model is applied, as detailed below [54–56]:

$$\mathbf{F}_{n,ij} = -k_n \delta_n \hat{\mathbf{n}}_{ij} - \eta_n v_n \hat{\mathbf{n}}_{ij}, \quad (10)$$

$$\mathbf{F}_{t,ij} = -\mu_s |\mathbf{F}_{n,ij}| \left(1 - \xi^{3/2} \right) \hat{\mathbf{t}}_{ij} - \gamma_t \sqrt{\frac{6m' \mu_s |\mathbf{F}_{n,ij}|}{\delta_{t,\max}}} \xi^{1/4} \mathbf{v}_t \hat{\mathbf{t}}_{ij}. \quad (11)$$

In Eq. (10), the stiffness and damping coefficients are defined as $k_n = \frac{4}{3} E' \sqrt{R' \delta_n}$ and $\eta_n = \gamma_n \sqrt{5m' k_n}$, respectively with γ_n being the damping ratio empirically ascertained using Schwager and Pöschel's method [57]. The variables v_n and \mathbf{v}_t are the normal and tangential components of the relative contact velocity and $\hat{\mathbf{t}}_{ij}$ the tangential unit vector aligned with the latter. The tangential component, given by Eq. (11), describes both elastic and frictional attributes through sticking and sliding, conditioned by a maximum tangential deformation related to the normal overlap, as described by $\delta_{t,\max} = (0.5 - v_i) / (1 - v_i) \mu_s \delta_n$ with μ_s denoting the particle friction coefficient. A specified factor, $\xi = 1 - \min(|\delta_t|, \delta_{t,\max}) / \delta_{t,\max}$, triggers sliding when $\delta_t > \delta_{t,\max}$ and causes the tangential force component to conform to Coulomb's law. The term $\gamma_t = \ln \varepsilon / \sqrt{\ln^2 \varepsilon + \pi^2}$ acts as the tangential damping ratio, akin to γ_n .

The thermal energy balance for solids, as expressed in Eq. (12), is predicated on the assumptions of a small Biot number and large Péclet numbers, which imply negligible internal temperature gradients and influence of conductive heat transfer via contacts [58,59]:

$$m_i c_{p,i} \frac{dT_i}{dt} = Q_{f,i} - \dot{m}_{v,i} \Delta H_{v,i}. \quad (12)$$

Within the specified equation, $c_{p,i}$ denotes the specific heat capacity of the solids, and $\Delta H_{v,i}$ signifies the latent heat of evaporation at the particle temperature. For the modelling of the spray process, liquid injections are introduced within a static spray zone situated above the nozzle. As particles traverse this spray, the coating solution is continuously administered at each DEM time step via particle enumeration and uniform distribution of liquid coating onto the particles [42,60]. In the simulations, only the solvent of pure water is sprayed, simplifying the quantification of the liquid coating volume received per passage by enabling its direct incorporation into the conservation equation for particle moisture content:

$$m_i \frac{dX_i}{dt} = \dot{m}_{v,i} + \dot{m}_{l,i}. \quad (13)$$

In this equation, X_i represents the moisture content of the particle, and $\dot{m}_{v,i}$ the rate of evaporation from the particle to the gas phase, as detailed in Section 2.2. The second term in Eq. (13), $\dot{m}_{l,i} = \dot{M}_l / N_p$, is calculated at each DEM time step exclusively for the N_p particles traversing the spray zone, based on the specified liquid spray rate \dot{M}_l . Notably, the added liquid mass is neglected in Eq. (8).

2.4. Coarse-graining technique

In this study, we apply a coarse-graining technique to formulate scaling laws as dimensionless groups Π_k , derived via dimensional analysis of the specified contact models, following established procedures documented in the literature [36–39]. The basis of this derivation is established on the dimensionless group $\Pi_1 = R_{cg} / R_o$, which signifies geometric similarity through the relationship between the radii of coarse-grained and original particles, denoted as R_{cg} and R_o , respectively. This group is subsequently recognised as the scaling factor or coarse-graining ratio ψ , which serves to quantify the level of coarse-graining by the number of original particles combined into each coarse-grained unit, as represented by ψ^3 . The selection process for ψ needs to account for the scaling of volume as $V_i \propto \psi^3$ and potential geometric constraints of the enclosing system while aiming to minimise the impact of particle size on overall bulk flow properties, thereby enabling the most efficient implementation.

In the dimensionless form of the Hertzian spring-dashpot contact model, previous literature [38,39] has demonstrated that for a constant relative overlap, the following dimensionless groups are identified:

$$\Pi_2 = \frac{k_n}{R' E'}, \quad \Pi_3 = \frac{\eta_n}{R'^2 \sqrt{\rho_i E'}}. \quad (14)$$

These groups, Π_2 and Π_3 , represent the scaling laws that must remain invariant to ensure mechanical similarity and conservation of energy density in accordance with the original system. Assuming ρ_i and E' are invariant, these dimensionless quantities elucidate the precise correspondence between the original and scaled systems, as specified by $k_{n,cg}/R_{cg} = k_{n,o}/R$ and $\eta_{n,cg}/R_{cg}^2 = \eta_{n,o}/R^2$. Provided that the coefficient of restitution remains constant, the energy dissipated in a binary collision of the coarse grains will correspond to ψ^3 collisions in the original system. Consequently, from the defined stiffness and damping coefficients, we find that $k_{n,cg} \propto \psi k_{n,o}$ and $\eta_{n,cg} \propto \psi^2 \eta_{n,o}$, demonstrating that Π_2 and Π_3 remain unaffected by the scaling. Notably, due to the size-independent packing of spheres, the voidage remains invariant during scaling [30]. Moreover, the DEM time step, set at 20% of the Rayleigh time, is proportional to R_i , thereby further accelerating the simulation process.

The scaling laws derived from Hertz normal contact force are consistent with Chialvo et al.'s findings [61], that the quasi-static granular pressure scales as $p_s \propto k_n/R_i$, suggesting invariant stresses. The relative scaling of this component, $F_{n,cg}/F_{n,o} \propto \psi^2$, extends to the Mindlin-Deresiewicz tangential contact force, provided that the friction coefficient, μ_s , remains unchanged. This consistent ψ^2 -scaling across both contact force components results in invariant stresses in all flow regimes, as substantiated by the analysis of the particle stress tensor:

$$\sigma_i = -\frac{1}{V_i} \left[m_i(\mathbf{u}_i - \bar{\mathbf{u}}) \otimes (\mathbf{u}_i - \bar{\mathbf{u}}) + \sum_j (F_{n,ij} + F_{t,ij}) \otimes I_{ij} \right]. \quad (15)$$

Here, $\bar{\mathbf{u}}$ represents the local mean velocity of the particles, while I_{ij} denotes the branch vector situated between the centres of mass of the colliding elements. From the quadratic scaling of contact forces, it becomes evident in Eq. (15) that $\sigma_i \neq f(\psi)$, such that the stresses are unaffected by the scaling process [37,38].

Having established the ψ^2 -scaling of contact forces, we shift our attention to the remaining force and heat transfer components in Eqs. (8) and (12), which, under similarity principles, must comply with $F_i \propto \psi^3$ and $Q_i \propto \psi^3$. While the body and pressure gradient forces naturally meet this criterion due to the ψ^3 -scaling of mass and volume, other terms do not inherently adhere to this scaling. Therefore, adjustments are required specifically for the drag force in Eq. (8), and for convective and evaporative heat transfer in Eq. (12) assuming that $c_{p,i}$ remains constant during scaling. Before implementing the necessary modifications to achieve ψ^3 -scaling for these terms, it is crucial to recognise that the empirical correlations used to compute the coefficients C_d , h , and h_c lack a theoretical foundation in the scaled system. To rectify this, we use the original particle size as the characteristic length in our calculations of the Reynolds, Nusselt, and Sherwood numbers, ensuring consistent values under identical conditions. As all particle-associated areas scale as $A \propto \psi^2$, we maintain system similarity by multiplying the drag force and the convective and evaporative heat transfers by a factor of ψ .

2.5. Assessment of rheology in granular flows

In rheological studies of granular flows, determining specific flow regimes and their transitional phases involves contrasting the macroscopic shear deformation timescale, $1/\dot{\gamma}_s$, to the particles' inertial timescale, $\sqrt{\rho_i d_i^2/p_s}$ [17,22,23]. This comparison yields a dimensionless parameter, the inertial number, as given in Eq. (16), which assesses whether the granular pressure p_s is sufficient for consolidating the particles or if the magnitude of the shear strain rate, $\dot{\gamma}_s$, is sufficiently high to cause dilation.

$$I = \frac{d_i \dot{\gamma}_s}{\sqrt{p_s/\rho_i}}. \quad (16)$$

In simulations and experiments of distinctive systems, both in terms of conditions and geometry, three different flow regimes are observed based on the relationship between the inertial number and the effective

Table 1

Physical and mechanical properties of the simulated MCC pellets.

Physical property	Numerical value
Particle diameter	1749 μm
Particle density	1420 kg m^{-3}
Young's modulus of particles	1 MPa
Poisson's ratio of particles	0.30
Poisson's ratio of walls	0.33
Particle-particle friction coefficient	0.53
Particle-wall friction coefficient	0.20
Particle-particle restitution coefficient	0.83
Particle-wall restitution coefficient	0.80

friction coefficient, defined as $\mu'_s = |\tau_s|/p_s$, which quantifies the macroscopic solid shear stress [24]. The quasi-static flow regime is characterised by its stress-rate independence, as indicated by a constant μ'_s , which has been identified at $I \lesssim 10^{-3} - 10^{-2}$. With an increased rate and inertia becoming influential, a rate-dependent pattern emerges, seen by a monotonic increase in μ'_s with I , defining the dense inertial flow regime. The transition into collisional flow, consistent with the kinetic theory postulations, is observed at $I \gtrsim 10^{-1} - 10^0$, where μ'_s exhibits a plateau [14,61]. Further details on deriving macroscopic granular continuum-equivalent properties from discrete particle data are presented in Appendix B.

3. Simulation setup

3.1. Experimental validation of numerical framework

In the present study, a GPU-CPU parallelised framework of two solvers was employed; Rocky DEM was executed on an NVIDIA Tesla V100 32 GB GPU, whereas the CFD in Fluent ran on Intel Xeon Gold 5220 CPUs, utilising 26 cores. A two-way data exchange between the solvers occurs at initialisation and at each CFD time step. All modifications related to coarse-graining are integrated within Rocky DEM, and the necessary function changes and source terms are loaded into Fluent through User-Defined Functions (UDFs).

We validate our CFD-DEM framework through comparison with experimental data from positron emission particle tracking (PEPT) [2] in a STREA-1 Wurster coater. In these experiments, for the 200 g batch of microcrystalline cellulose (MCC), single pellets labelled with the radioisotope Fluorine-18 were monitored over an extended period. This procedure yielded data on particle velocity, residence time (RT) per passage, and cycle time (CT) distribution.

The material properties of the MCC pellets used in the simulations, which reflect the relatively large and porous nature of the pellets employed in the PEPT experiments, are detailed in Table 1. System-specific details and dimensions of the STREA-1 coater are provided in [2], whereas simulation-specific parameters can be found in [3,25], wherein CFD-DEM was employed with the MultiFlow solver for validation against the PEPT data. Similarly, Böhlinger et al. validated their CFD-DEM framework using the XPS/AVL-Fire solver [9], offering dual reference points for a comparative assessment of our CFD-DEM framework. Consequently, we will juxtapose the simulated values with the experimental data reported in [2] and the aforementioned CFD-DEM studies [3,9,25].

3.2. System adaptation and coarse-graining design

Building on the system settings outlined in the previous section, this section incorporates three levels of coarse-graining ($\psi = 2, 3, 4$), in addition to the original particle system ($\psi = 1$), achieved by grouping sets of 8, 27 and 64 original particles into coarse grains. For an accurate evaluation, we aim to minimise the influence of the coarse grain size on bulk properties. Accordingly, the original particle size is determined by ensuring the diameter of the coarsest grains ($\psi = 4$) does not

Table 2
Simulation parameters.

Framework	Numerical value
DEM	
Scaling factor	1, 2, 3, 4
Particle diameter	375, 750, 1125, 1500 μm
Particle count	5.1, 0.64, 0.19, 0.08 M
Time step	7.7, 15.5, 22.3, 30.1 μs
CFD	
Time step	1×10^{-4} s
<i>Fluidising gas inlet:</i>	
Velocity inner annulus	2.01 m s^{-1}
Velocity outer annulus	0.41 m s^{-1}
Temperature	50 $^{\circ}\text{C}$
Relative humidity	6%
<i>Atomising gas inlet:</i>	
Velocity	45 m s^{-1}
Temperature	20 $^{\circ}\text{C}$
Relative humidity	6%
Spray	
Liquid spray rate	10 g min^{-1}
Water density	998 kg m^{-3}

exceed one-tenth of the partition gap. This is the narrowest gap in the geometry, defined as the distance between the tube and the distributor plate. Following this criterion, the diameter of the coarsest grains is 1500 μm for $\psi = 4$, which defines the original particle size as $d_o = (1500 \mu\text{m})/4 = 375 \mu\text{m}$.

In Section 4.2, we transition from using larger Geldart type D particles employed in the validation (Section 4.1) to significantly smaller Geldart type B particles. This necessitates inlet airflow adjustments to mitigate excessive particle collisions at the outlet boundary and slugging fluidisation. Consequently, we reduce the atomising gas velocity from 50 to 45 m/s and adjust the fluidising gas flow according to Ergun’s equation (see, e.g., [62]), ensuring a consistent pressure drop across the bed. Revised gas-phase inlet conditions, including air humidity, and modelling parameters for the spray zone and coarse-graining sequence are detailed in Table 2. Heat losses to the environment at 20 $^{\circ}\text{C}$ are quantified using a wall heat transfer coefficient of 30 $\text{W m}^{-2} \text{K}^{-1}$, as per the method in [48] for a Glatt GPCG-2 6'' Wurster coater. The specific heat capacity of the particles, 200 $\text{J kg}^{-1} \text{K}^{-1}$, follows the data for MCC pellets in [5].

4. Results and discussion

4.1. Experimental validation of CFD-DEM framework

Before the application of the scaling technique ($\psi > 1$), the CFD-DEM framework in its original, unscaled form ($\psi = 1$) is validated by contrasting it to the experimental data presented in [2] and comparing it against simulated values reported in two separate publications [3,9].

Vertical particle velocities measured 90 mm above the distributor plate using PEPT, alongside their corresponding time-averaged values derived from simulations, are depicted in Fig. 2. The agreement between the simulated and the experimental particle velocities is evident. The negative velocity at the interior wall of the tube quantifies the prevalence of particles undergoing recirculation within the tube [2]. We present the average particle residence time (RT) per passage through the delineated regions in Fig. 3. The simulated RTs within the tube and drying regions exhibit close alignment with PEPT predictions. Previous studies have highlighted a pronounced underestimation of simulated RTs in the bed region. Conversely, our simulated RT in this region corresponds with the experimental values.

Fig. 4 illustrates the corresponding particle cycle time (CT) distributions, deduced from a 30 s simulation, which includes only recorded

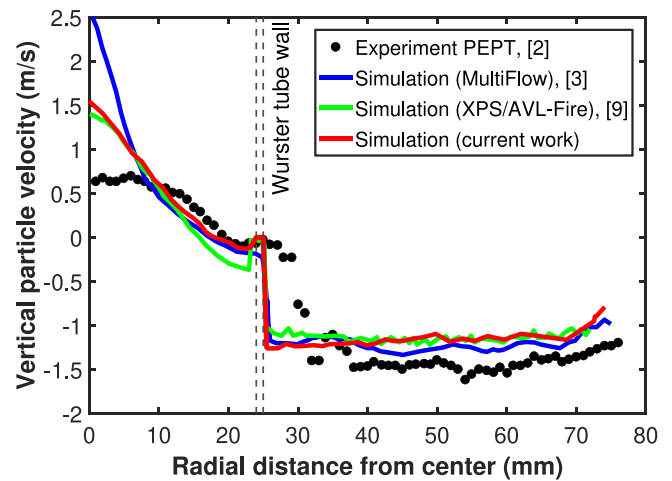


Fig. 2. Time-averaged vertical velocity profiles of particles, measured 90 mm above the distributor plate, juxtaposing experimental data from PEPT [2] with simulation outcomes from this study and those reported in [3,9].

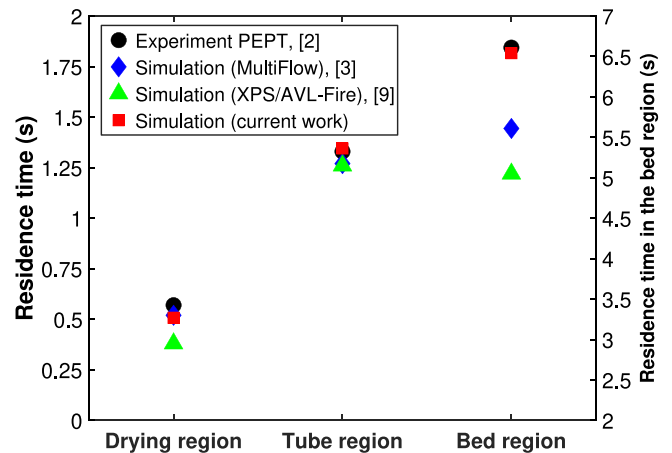


Fig. 3. Average particle residence times, per cycle, in the distinct zones of the Wurster coater, as determined by the PEPT experiment [2] and simulations presented in both the current and referenced papers [3,9].

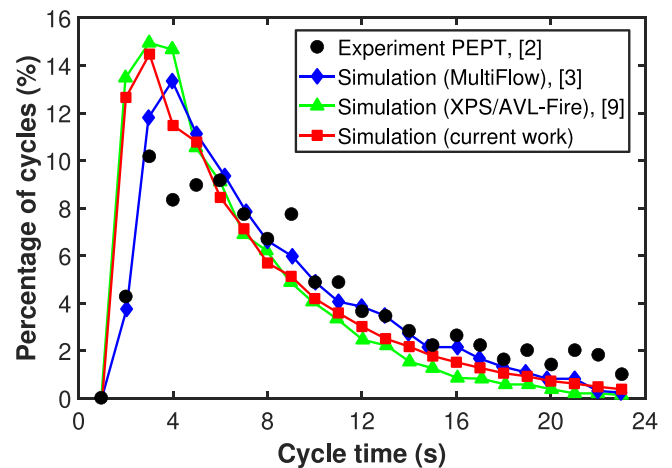


Fig. 4. Particle CTs distribution, limited to cycles shorter than 25 s, obtained from experimental data [2], simulation results of the present study, and findings from referenced papers [3,9].

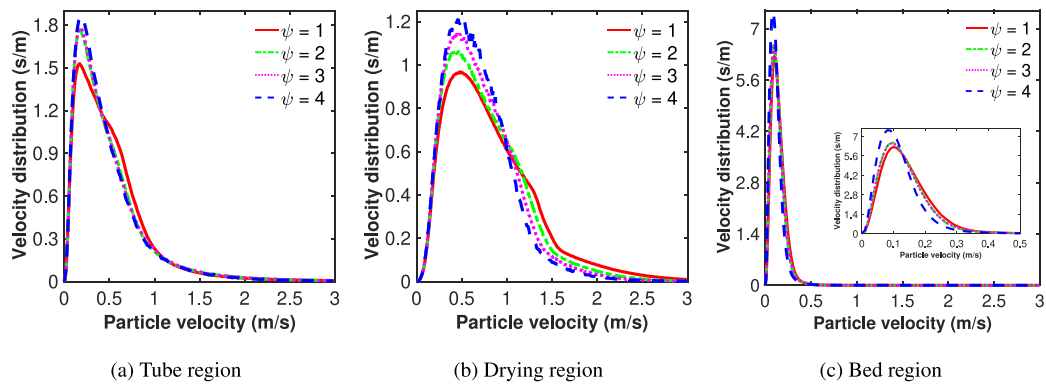


Fig. 5. Probability distributions of particle velocities in the tube (a), drying (b), and bed (c) regions in the original particle system ($\psi = 1$) and the coarse-grained systems ($\psi = 2, 3, 4$). The inset provides an improved visual of the shift in velocities across the bed.

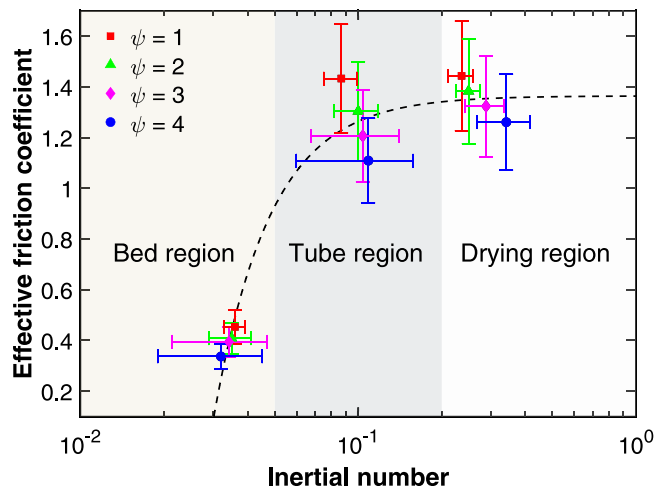


Fig. 6. Time-volume averaged effective friction coefficients and inertial numbers across regions for original ($\psi = 1$) and scaled systems ($\psi = 2, 3, 4$). Standard deviations are represented by error bars, and the dashed line delineates the observed trend.

particle cycles shorter than 25 s. A consistent trend across the simulations is apparent, wherein cycles shorter than 5 s are overestimated, while longer cycles are underestimated. In this study, the RTs suggest a heavier tail in the CT distribution relative to other simulations. However, the CTs presented by Li et al. contradict this expectation, possibly owing to their observation of a stable distribution in the simulations exceeding 25 s [3]. In contrast, this stability was not observed in our simulations, where the CT distribution showed a consistent trend towards longer cycle times for simulations extending from 25 to 30 s. This indicates the necessity for longer simulations to achieve a stable distribution with longer RTs. Nevertheless, the predictions with the current CFD-DEM framework already show good concordance with the experimental observations, thus negating the need for extended simulations.

4.2. Coarse-graining with heat and mass transfer integration

4.2.1. Dynamics of particle motion and momentum

To assess the effects of progressive coarse-graining on momentum and motion relative to the unscaled system, simulations spanning 20 s were conducted under isothermal conditions. During this period, particle data from designated regions were extracted at 0.05-s intervals, yielding a total of 400 samples. The choice of sampling frequency and simulation duration was strategically aimed at mitigating statistical bias, which arises from increased variance in coarse-grained systems due to the limited number of particles contributing data in each sample.

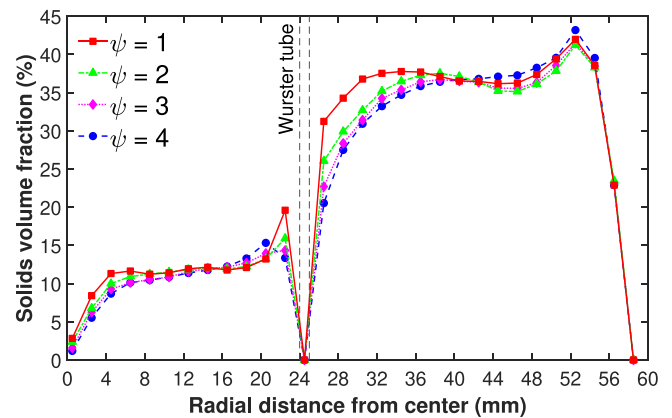


Fig. 7. Solids volume fraction profiles radially in a 10 mm cross-section, located 15 mm above the distributor plate (lower section of the tube, adjacent to the lower tube entry), segmented into 2 mm radial increments, showcased for the unscaled ($\psi = 1$) and scaled ($\psi = 2, 3, 4$) systems.

In Fig. 5, we introduce the unfiltered particle velocity probability distribution functions for each region, evaluated based on all recorded particle values in each sample. In the tube, coarse-graining induces a shift towards marginally lower velocities, a trend consequently mirrored in the drying region. However, the shift in the drying region is more marked, attributable to two factors: firstly, the occurrence of the elevated velocities originating from the tube that, secondly, cause particles to ascend higher before descending, thus enhancing the downward velocities due to increased falling heights. In the bed region, results are almost identical, except for the coarsest grains, which exhibit marginally lower velocities. The latter is depicted for clarity in an inset of Fig. 5.

The time-volume averaged inertial numbers and corresponding effective friction coefficients for each region are given in Fig. 6. The bed region exhibits a dense inertial regime, as evidenced by its inertial number and the mean ratio of relative collisional to frictional stress, approximately 0.65, reducing to about 0.57 for the coarsest grains. Conversely, the tube and drying regions demonstrate a dominant collisional flow regime, indicated by negligible frictional components of solid stresses and higher inertial numbers. This regime is further identified by the values of μ'_s , which saturate due to the high shear stress relative to confining pressure. An increase in ψ correlates with an earlier saturation of μ'_s and the more pronounced variability in inertial numbers.

We present in Fig. 7 the radial distribution of the solid volume fraction within a cross-section 15 mm above the distributor plate. Near the internal tube wall, the elevated solid concentrations in the original

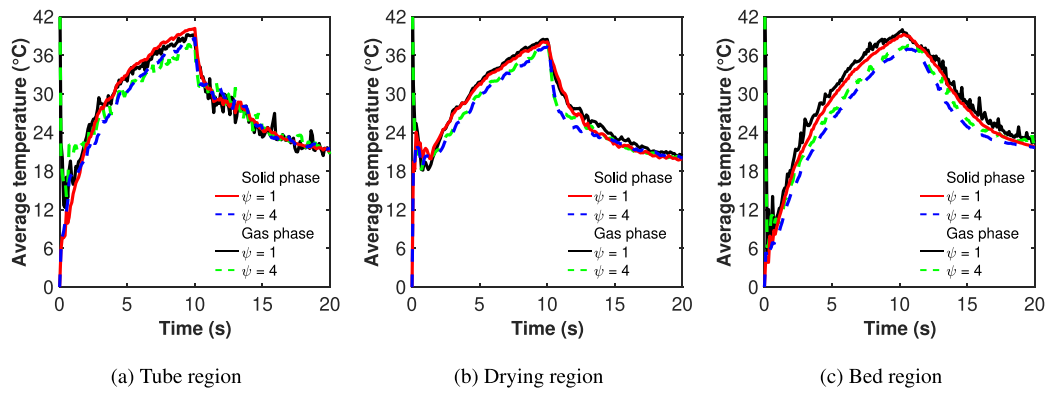


Fig. 8. Transient profiles of the gas and solid phases' mean temperatures in each region over 20 s for the original particle system ($\psi = 1$) and the systems with the coarsest grains ($\psi = 4$).

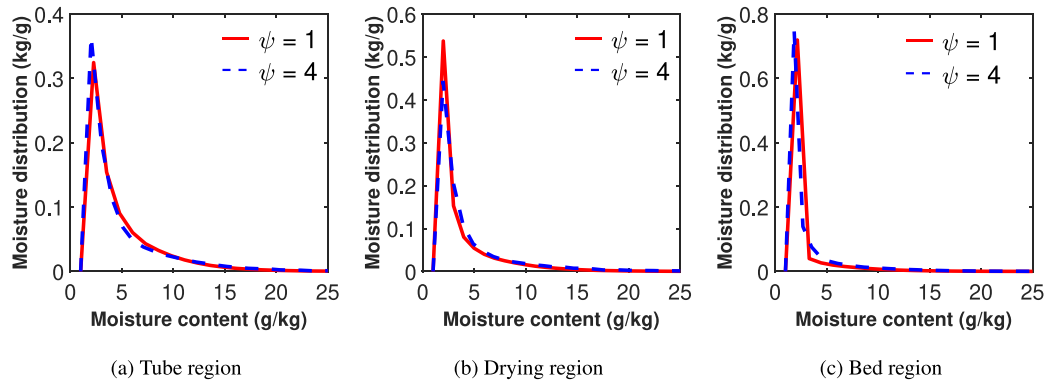


Fig. 9. Moisture probability distribution function in each region after 20 s for the original particle system ($\psi = 1$) and the systems with the coarsest grains ($\psi = 4$). Values are presented in grams of liquid per kilogram of solid.

particle system cause steeper radial gradients, promoting the Venturi effect. Although the velocity profile remains largely unchanged, see Appendix C, there is an appreciable increase in the air mass flow towards the tube centre, resulting from the fluidising gas entering the tube closer to the jet. Counter-intuitively, the total airflow via the tube remains close, owing to the higher axial flow of fluidising gas along the tube walls in the coarse-grained systems. The milder radial gradients at the tube entry further promote the amount of gas flowing along the external tube side, as indicated in the outer annular region in the solids volume fraction of Fig. 7, caused by more rigorous fluidisation. In the coarsest system, this observation becomes consequential, as solids begin to concentrate radially outward in the bed. The implication is that the grain size becomes influential in the bed region when $\psi = 4$, as indicated by the shift in the velocity distribution. Furthermore, this accounts for the observed higher confining pressure in correlation with the lower effective friction coefficient in the bed.

In examining the characteristics of the flow regime, our findings reliably reproduce macroscopic properties of granular flow in coarse-grained systems. Deviations are predominantly localised within the tube, ascribed to the heightened intake of fluidising air closer to the centre at lower values of ψ . Concurrently, the horizontal transport of particles in the bed is enhanced, as indicated by the elevated particle concentration towards the centre. This is likely a consequence of smaller particles tending to pack more densely near the walls, suggesting a potential geometric limitation dictated by the particle size to the confining dimensions. Determining whether this is solely a geometric constraint or a result of a combination of various factors requires further evaluation. To address this question, it is probably needed to employ a coarse-graining procedure in a larger Wurster coater geometry. Such an effort is outside the scope of the present work.

4.3. Thermal and mass transfer dynamics

To ascertain the accuracy of integrating heat and mass transfer phenomena in a coarse-grained system, a dynamic two-stage analysis was conducted. This involved 20-s simulations comparing the system with the highest degree of coarse-graining ($\psi = 4$) against the original system ($\psi = 1$). Initiating the simulations from a packed bed configuration with a uniform (dry) particle temperature of 0 °C, the first stage, lasting 10 s, involve convective heating of the particles with hot fluidising air. The subsequent stage introduces the spray, where pure water is injected at a constant rate.

The regionally averaged gas and solid phase temperature profiles over 20 s, encompassing the convective and spray stages consecutively, are depicted in Fig. 8. The temperatures closely align, with the original particle system remaining only marginally warmer. The most pronounced difference is observed during the bed's heating-up stage, wherein the gas temperatures of the system diverge by some 2.6 °C after 10 s. In this initial stage, a gradual convergence over time is noted, yet it does not reach a plateau before the onset of the second stage, indicating a trend towards converging steady-state temperatures. In the ensuing spray stage, the system temperatures rapidly converge, culminating in near-identical conditions with a maximum difference below 0.5 °C after 20 s.

After the spray phase ($t = 20$ s), the moisture probability distribution functions are compared in each region of both the original and scaled systems. These are presented in Fig. 9 and demonstrate high consistency, indicating nearly identical drying behaviour with each region exhibiting a log-normal distribution. The conforming phase temperatures in both systems indicate effective mixing, suggesting that the slower response in the scaled system during the heating stage is attributed to the previously described differences in the fluidising gas distribution. When $\psi = 1$, the augmented Venturi effect enhances

the efficiency of convective heat transfer by drawing additional hot air towards the centre from the peripheral areas of the distributor plate. This mechanism facilitates improved heating coverage of solids, resulting in an elevation of the average temperature within the bed region, which subsequently propagates into the tube and drying regions. Nonetheless, the coarse-grained system's proficiency in mirroring the thermal response, even under dynamically varying conditions, along with its analogous drying properties and the attainment of consistent moisture distribution, exemplifies a significant level of alignment.

4.4. Directions on the upper limit of coarse-graining in Wurster coaters

It is of interest to discuss the optimal degree of coarse-graining for a certain system. In the examined system, the greatest deviations were observed at the tube's entry, in connection with the partition gap, which serves as the narrowest gap in the geometry and thereby dictates the maximum particle size that can effectively pass through. We chose this gap as a reference point for determining the largest dimensions of the coarse grains, setting it to correspond to 10% of this gap for the largest value of ψ , which was determined by the number of particles deemed practical for simulation. Combining these outcomes, we conclude that the geometry of the Wurster coater sets the upper coarse-graining limit. Hence, supported by the results, we suggest that the diameter of the coarse grains should not exceed 10% of the partition gap. This provides a useful guideline for the a priori selection of ψ .

As tube and partition gap dimensions increase in larger systems, we expect that higher values of ψ will be applicable while maintaining the same level of numerical uncertainty associated with coarse-graining, as demonstrated in fluidised beds [63]. Additionally, significantly higher ψ values have been experimentally validated in large-scale units such as catalytic crackers, cyclones, and circulating fluidised beds [64], reaching up to $\psi = 60$ [65]. However, such values of ψ do not align with the specific geometric constraints observed in our system. For 18" Wurster tube insets and larger, where the partition gap typically ranges from 35–60 mm [10], the resulting coarse grain sizes would correspond to 38%–64% of the partition gap. Based on these findings, we recommend a scaling factor of ψ between 8 and 16 for larger units equipped with the 18" Wurster inset.

4.5. Computational implications

For the simulations of the original CFD-DEM system ($\psi = 1$), each second of simulation output necessitated 12 h of real-time computation. In contrast, the equivalent system employing coarse-graining with $\psi = 4$ demonstrated a ten-fold increase, accomplishing 10 s of simulation within the same period, thus presenting a logarithmic reduction in computational time. It should be noted that with $\psi = 4$, the limited number of tracked elements meant that the CFD, rather than the DEM, controls the simulation speed, thus preventing further observable reductions in computational time. Nonetheless, this suggests that the adopted scaling approach ensures at least a logarithmic decrease in computational time in scenarios where DEM computations on GPUs control the simulation pace, as is typically the case in real process-scale systems.

5. Conclusions

This study presents simulations of the Wurster coating process using CFD-Discrete Element Modelling, both with and without integrating a coarse-graining technique. By implementing the coarse-graining technique and significantly reducing the particle count, we demonstrate that the obtained results closely resemble those in the unscaled CFD-DEM system while achieving a logarithmic enhancement in simulation speed. Experimental validation using PEPT data confirmed the accuracy in particle velocities, residence times and cycle time distributions.

The coarse-graining technique accurately reproduced the macroscopic granular flow properties, albeit with slight discrepancies in the tube region attributable to the influence of grain size on the gas flow distribution within and outside the tube. By integrating spray modelling and considering air humidity, we were able to comprehensively investigate the heat and mass transfer processes in the coarse-grained, including the transient phase temperature profiles and moisture distributions. This allowed us to demonstrate the coarse-grained system's capability to predict near identical moisture uniformity and thermal response as the original system.

The reduction in particle count achieved through coarse-graining, whilst retaining a close corresponding level of resolution, highlights the potential to overcome existing computational constraints of CFD-DEM. This advancement facilitates the feasibility of conducting simulations of Wurster coater systems on an industrial scale.

CRediT authorship contribution statement

Philip Kjaer Jepsen: Writing – review & editing, Writing – original draft, Visualization, Validation, Software, Methodology, Investigation, Conceptualization. **Luis Martin De Juan:** Writing – review & editing, Supervision, Conceptualization. **Astrid Boje:** Writing – review, Conceptualization. **Sohan Sarangi:** Writing – review, Conceptualization. **Christian von Corswant:** Writing – review, Conceptualization. **Srdjan Sasic:** Writing – review, Supervision, Methodology, Investigation, Conceptualization.

Declaration of competing interest

The authors declare that they have no known competing financial interests or personal relationships that could have appeared to influence the work reported in this paper.

Data availability

The authors do not have permission to share data.

Acknowledgements

The authors extend their sincere gratitude to Hans Carlsson for his support and detailed guidance on experimental procedures. Special thanks are due to Mats Johansson for providing thorough descriptions of the Wurster coater system utilised in the PEPT experiments, which supplied the data used for this study's validation. Additionally, the authors acknowledge AstraZeneca R&D, Mölndal, Sweden, for supplying the computational resources and infrastructural support essential for this research.

Appendix A. Implementation of diffusion-based particle redistribution method

The redistribution method can be implemented by iteratively solving a discretised form of the diffusion equation to redistribute excessive solid fractions from high-concentration cells to neighbouring cells. The transferred quantity is then calculated based on the difference in the solid fraction between the neighbouring cells, and the iteration continues until the specified maximum solid volume fraction or the maximum number of iterations is reached. An explicit form of Fick's second law of diffusion is obtained by assuming a homogeneous allocation of the computational cells. Then, the discretised diffusion equation that computes the new concentration α_c after diffusion from an initial concentration α_{c_0} , provided by the PCM, to N neighbouring cells can be expressed as follows:

$$\alpha_c = \alpha_{c_0} + \frac{\Omega}{V_c} \sum_{n \in N} (\alpha_n - \alpha_{c,0}) \quad (\text{A.1})$$

The constant Ω is proportional to the diffusion constant and determines the iteration rate of the solid volume fraction. A greater Ω leads to faster iterations, but can compromise stability. In a non-uniform Eulerian grid, the value of Ω only needs to be the same within the sets of cells that exchange solid volume fractions. Thus, an optimal value of Ω is determined per cell as $\Omega = V_c/2N$, which if substituted into (A.1) gives Eq. (A.2) below, that represents the maximum rate at which the cell can undergo a stable exchange:

$$\alpha_c = \alpha_{c_0} + \frac{1}{2N} \sum_{n \in N} (\alpha_n - \alpha_{c_0}). \quad (\text{A.2})$$

Therefore, for any set of exchanging cells, if a neighbouring cell has a lower value of Ω_n , this value must be adopted for summation over all these cells, thus restricting the overall diffusion rate for that set. By implementing this knowledge, Eq. (A.1) can be expressed as follows:

$$\alpha_c = \alpha_{c_0} + \frac{1}{V_c} \sum_{n \in N} \min[\Omega_n, \Omega] (\alpha_n - \alpha_{c_0}). \quad (\text{A.3})$$

The presented equation is applied to every cell within the Eulerian domain and solved iteratively to obtain the updated value of α_c in each cell during the mapping process of solid volume fraction between the Lagrangian and Eulerian frameworks. Additionally, the diffusion of solid volume fraction is employed to facilitate the mapping of energy and momentum exchange, with additional weighting based on the fluid volume present in the current cell at a specific time [49,51]. The application of the method to other quantities is analogous. For

smoothing of a given force component F_{c_0} , the new force is obtained by:

$$F_c = F_{c_0} + \frac{1}{V_c} \sum_{n \in N} \min[\rho_n \Omega_n, \rho \Omega] \left(\frac{F_n}{\rho_n} - \frac{F_{c_0}}{\rho} \right). \quad (\text{A.4})$$

Seen from Eq. (A.4), the force components are weighted by the specific mass of gas occupying the cells. Conversely, for heat transfer:

$$Q_c = Q_{c_0} + \frac{1}{V_c} \sum_{n \in N} \min[\rho_n c_{p,n} \Omega_n, \rho c_p \Omega] \left(\frac{Q_n}{\rho_n c_{p,n}} - \frac{Q_{c_0}}{\rho c_p} \right). \quad (\text{A.5})$$

Appendix B. Macroscopic solids stresses and strains

To study the collective granular material behaviour at a macroscopic scale, the transition from discrete particle stresses to a continuum-based framework necessitates considering a control volume $V_s \gg V_i$. The macroscopic stress tensor of the granular assemblies, σ_s , is calculated as the volume-averaged sum of the stresses of the individual particles, given by $\sigma_s = \sum_i \sigma_i V_i / V$. The granular pressure, p_s , is derived from the isotropic part of this tensor as $p_s = tr(\sigma_s) / 3$. The magnitude of shear stresses, $|\tau_s|$, is obtained from the second invariant of the deviatoric part of σ_s , and their ratio defines the effective or bulk friction coefficient $\mu'_s = |\tau_s| / p_s$. The shear strain rate magnitude, $\dot{\gamma}_s$, is determined from the deviatoric part of the macroscopic granular strain rate tensor, D_s^{dev} , as $\dot{\gamma}_s = 2 \|D_s^{dev}\|$.

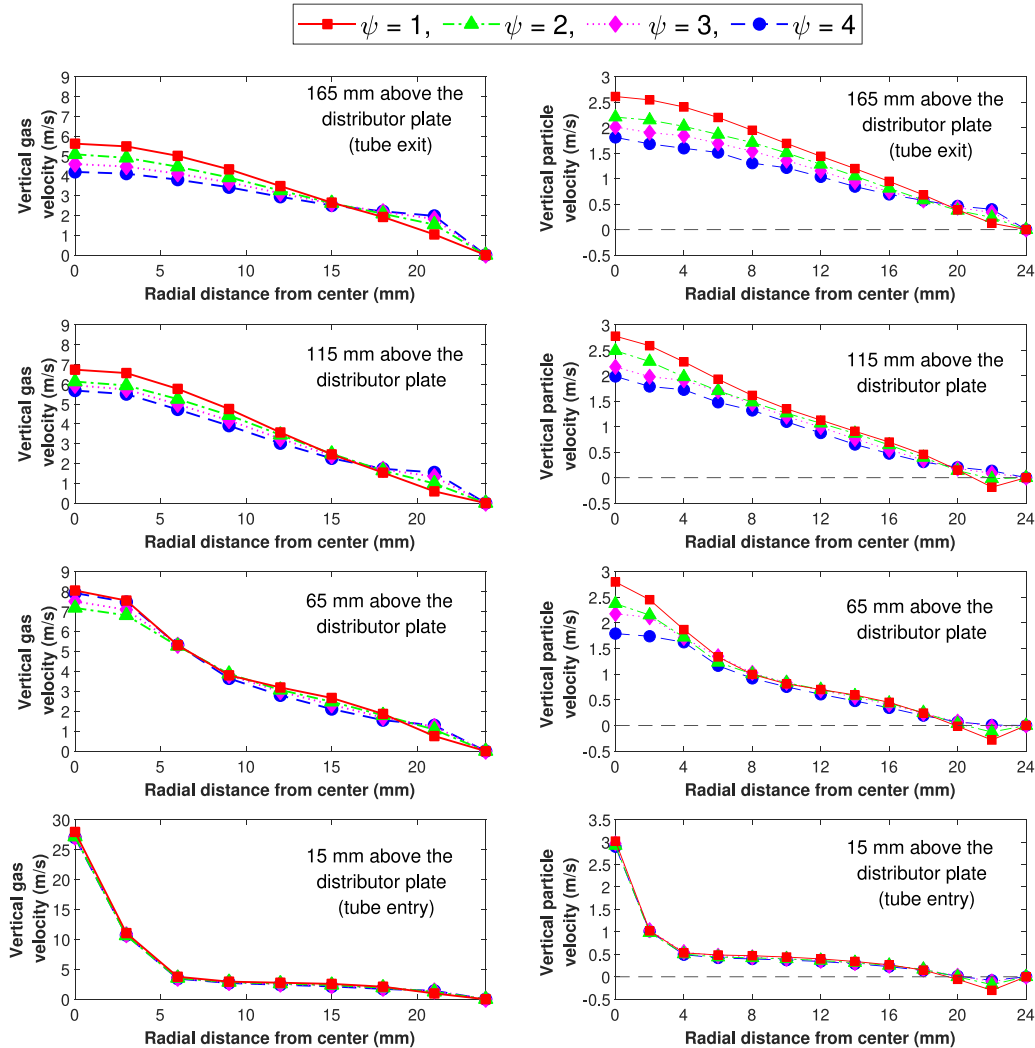


Fig. C.10. Radial vertical velocities of gas and solids across four different segments within the tube, shown for both the original ($\psi = 1$) and scaled systems ($\psi = 2, 3, 4$).

Appendix C. Radial velocity profiles in the Wurster tube

In Fig. C.10, we detail the time-volume averaged vertical velocity profiles of gas and particles, arranged radially across four sections of the tube, each 4 mm in height. In the initial section, at the tube's entry, the gas's vertical velocity exhibits minimal variation. However, the deviations become increasingly apparent in the upper sections, particularly near the walls, for particle velocities. Here, less negative velocities indicate reduced internal particle circulation in the original system. This phenomenon is attributed to diminished airflow at a distance from the centre in the original configuration, underscoring the radial disparity in airflow concerning the fluidising gas.

References

- [1] K.-S. Seo, R. Bajracharya, S.H. Lee, H.-K. Han, Pharmaceutical application of tablet film coating, *Pharmaceutics* 12 (9) (2020) 853, <http://dx.doi.org/10.3390/pharmaceutics12090853>.
- [2] L. Li, A. Rasmuson, A. Ingram, M. Johansson, J. Rimmelgas, C. von Corswant, S. Folestad, PEPT study of particle cycle and residence time distributions in a Wurster fluid bed, *AIChE J.* 61 (3) (2015) 756–768, <http://dx.doi.org/10.1002/aic.14692>.
- [3] L. Li, J. Rimmelgas, B.G. van Wachem, C. von Corswant, M. Johansson, S. Folestad, A. Rasmuson, Residence time distributions of different size particles in the spray zone of a Wurster fluid bed studied using DEM-CFD, *Powder Technol.* 280 (2015) 124–134, <http://dx.doi.org/10.1016/j.powtec.2015.04.031>.
- [4] L. Fries, S. Antonyuk, S. Heinrich, S. Palzer, DEM-CFD modeling of a fluidized bed spray granulator, *Chem. Eng. Sci.* 66 (11) (2011) 2340–2355, <http://dx.doi.org/10.1016/j.ces.2011.02.038>.
- [5] M. Trogrić, S. Madlmeir, T. Forgber, S. Salar-Behzadi, A. Sarkar, P. Liu, L. Contreras, A. Carmody, A. Kape, J. Khinast, D. Jajčević, Numerical and experimental validation of a detailed non-isothermal DEM-CFD model of a pilot-scale Wurster coater, *Powder Technol.* 391 (2021) 97–113, <http://dx.doi.org/10.1016/j.powtec.2021.05.100>.
- [6] C. Frey, Chapter 8 - Fluid bed coating-based microencapsulation, in: R. Sobel (Ed.), *Microencapsulation in the Food Industry* (Second Edition), second ed., Academic Press, 2023, pp. 83–115, <http://dx.doi.org/10.1016/B978-0-12-821683-5.00024-8>.
- [7] M. Foroughi-Dahr, R. Sotudeh-Gharebagh, N. Mostoufi, Development of a PAT tool for monitoring the Wurster coater performance, *Int. J. Pharm.* 561 (2019) 171–186, <http://dx.doi.org/10.1016/j.ijpharm.2019.02.023>.
- [8] Y. Song, T. Zhou, R. Bai, M. Zhang, H. Yang, Effect of operational and geometric parameters on the hydrodynamics of a Wurster coater: A DEM-CFD study, *Particuology* 85 (2024) 62–76, <http://dx.doi.org/10.1016/j.partic.2023.03.019>.
- [9] P. Böhring, J.G. Khinast, D. Jajcevic, C. Davies, A. Carmody, P. Doshi, M.T. Am Ende, A. Sarkar, Computational fluid dynamics-discrete element method modeling of an industrial-scale Wurster coater, *J. Pharm. Sci.* 108 (1) (2019) 538–550, <http://dx.doi.org/10.1016/j.xphs.2018.10.016>.
- [10] D. Jones, E. Godek, Chapter 35 - development, optimization, and scale-up of process parameters: Wurster coating, in: Y. Qiu, Y. Chen, G.G. Zhang, L. Yu, R.V. Mantri (Eds.), *Developing Solid Oral Dosage Forms* (Second Edition), second ed., Academic Press, Boston, 2017, pp. 997–1014, <http://dx.doi.org/10.1016/B978-0-12-802447-8.00035-2>.
- [11] A. Zhu, Q. Chang, J. Xu, W. Ge, A dynamic load balancing algorithm for CFD-DEM simulation with CPU-GPU heterogeneous computing, *Powder Technol.* 428 (2023) 118782, <http://dx.doi.org/10.1016/j.powtec.2023.118782>.
- [12] D. Jajcevic, E. Siegmann, C. Radeke, J.G. Khinast, Large-scale CFD-DEM simulations of fluidized granular systems, *Chem. Eng. Sci.* 98 (2013) 298–310, <http://dx.doi.org/10.1016/j.ces.2013.05.014>.
- [13] R. Šibanc, S. Srčić, R. Dreu, Numerical simulation of two-phase flow in a Wurster coating chamber and comparison with experimental results, *Chem. Eng. Sci.* 99 (2013) 225–237, <http://dx.doi.org/10.1016/j.ces.2013.05.057>.
- [14] S. Schneiderbauer, A. Aigner, S. Pirker, A comprehensive frictional-kinetic model for gas-particle flows: Analysis of fluidized and moving bed regimes, *Chem. Eng. Sci.* 80 (2012) 279–292, <http://dx.doi.org/10.1016/j.ces.2012.06.041>.
- [15] P.A. Cundall, O.D.L. Strack, A discrete numerical model for granular assemblies, *Géotechnique* 29 (1) (1979) 47–65, <http://dx.doi.org/10.1680/geot.1979.29.1.47>.
- [16] H. Li, D. Liu, J. Ma, X. Chen, Simulation of a Wurster fluidized bed by CFD-DEM with a cohesive contact model, *Chem. Eng. Res. Des.* 177 (2022) 157–166, <http://dx.doi.org/10.1016/j.cherd.2021.10.038>.
- [17] S. Chialvo, S. Sundaresan, A modified kinetic theory for frictional granular flows in dense and dilute regimes, *Phys. Fluids* 25 (7) (2013) 070603, <http://dx.doi.org/10.1063/1.4812804>.
- [18] N. Deen, M. Van Sint Annaland, M. Van der Hoef, J. Kuipers, Review of discrete particle modeling of fluidized beds, *Chem. Eng. Sci.* 62 (1) (2007) 28–44, <http://dx.doi.org/10.1016/j.ces.2006.08.014>.
- [19] H.M. Jaeger, S.R. Nagel, R.P. Behringer, Granular solids, liquids, and gases, *Rev. Mod. Phys.* 68 (1996) 1259–1273, <http://dx.doi.org/10.1103/RevModPhys.68.1259>.
- [20] C.S. Campbell, Granular material flows – An overview, *Powder Technol.* 162 (3) (2006) 208–229, <http://dx.doi.org/10.1016/j.powtec.2005.12.008>.
- [21] O. Pouliquen, C. Cassar, P. Jop, Y. Forterre, M. Nicolas, Flow of dense granular material: towards simple constitutive laws, *J. Stat. Mech. Theory Exp.* 2006 (07) (2006) P07020, <http://dx.doi.org/10.1088/1742-5468/2006/07/P07020>.
- [22] P. Jop, Y. Forterre, O. Pouliquen, A constitutive law for dense granular flows, *Nature* 441 (2006) 727–730, <http://dx.doi.org/10.1038/nature04801>.
- [23] F. da Cruz, S. Emam, M. Prochnow, J.-N. Roux, F. Chevoir, Rheophysics of dense granular materials: Discrete simulation of plane shear flows, *Phys. Rev. E* 72 (2005) 021309, <http://dx.doi.org/10.1103/PhysRevE.72.021309>.
- [24] G. MiDi, On dense granular flows, *Eur. Phys. J. E* (2004) 341–365, <http://dx.doi.org/10.1140/epje/i2003-10153-0>.
- [25] L. Li, J. Rimmelgas, B.G. van Wachem, C. von Corswant, S. Folestad, M. Johansson, A. Rasmuson, Effect of drag models on residence time distributions of particles in a Wurster fluidized bed: A DEM-CFD study, *KONA Powder Part. J.* 33 (2016) 264–277, <http://dx.doi.org/10.14356/kona.2016008>.
- [26] M.J.A. de Munck, E.A.J.F. Peters, J.A.M. Kuipers, DEM-CFD fluidized bed drying study using a coarse-graining technique, *Ind. Eng. Chem. Res.* 62 (48) (2023) 20911–20920, <http://dx.doi.org/10.1021/acs.iecr.3c02960>.
- [27] J. Hilton, D. Ying, P. Cleary, Modelling spray coating using a combined CFD-DEM and spherical harmonic formulation, *Chem. Eng. Sci.* 99 (2013) 141–160, <http://dx.doi.org/10.1016/j.ces.2013.05.051>.
- [28] H.R. Norouzi, Simulation of pellet coating in Wurster coaters, *Int. J. Pharm.* 590 (2020) 119931, <http://dx.doi.org/10.1016/j.ijpharm.2020.119931>.
- [29] P. Liu, C.M. Hrenya, Challenges of DEM: I. Competing bottlenecks in parallelization of gas-solid flows, *Powder Technol.* 264 (2014) 620–626, <http://dx.doi.org/10.1016/j.powtec.2014.04.095>.
- [30] A. Di Renzo, E.S. Napolitano, F.P. Di Maio, Coarse-grain DEM modelling in fluidized bed simulation: A review, *Processes* 9 (2) (2021) <http://dx.doi.org/10.3390/pr9020279>.
- [31] D. Owen, J. Loughran, On upscaling of discrete element models: Similarity principles, *Eng. Comput.: Int. J. Comput.-Aided Eng.* 26 (2009) 599–609, <http://dx.doi.org/10.1108/02644400910975405>.
- [32] Y. Feng, D. Owen, Discrete element modelling of large scale particle systems - I: Exact scaling laws, *Comput. Part. Mech.* 1 (2014) 159–168, <http://dx.doi.org/10.1007/s40571-014-0010-y>.
- [33] M. Sakai, S. Koshizuka, Large-scale discrete element modeling in pneumatic conveying, *Chem. Eng. Sci.* 64 (3) (2009) 533–539, <http://dx.doi.org/10.1016/j.ces.2008.10.003>.
- [34] K. Washino, E.L. Chan, T. Kaji, Y. Matsuno, T. Tanaka, On large scale CFD-DEM simulation for gas-liquid-solid three-phase flows, *Particuology* 59 (2021) 2–15, <http://dx.doi.org/10.1016/j.partic.2020.05.006>.
- [35] M. Sakai, H. Takahashi, C.C. Pain, J.-P. Latham, J. Xiang, Study on a large-scale discrete element model for fine particles in a fluidized bed, *Adv. Powder Technol.* 23 (5) (2012) 673–681, <http://dx.doi.org/10.1016/j.apt.2011.08.006>.
- [36] D.S. Nasato, C. Goniva, S. Pirker, C. Kloss, Coarse graining for large-scale DEM simulations of particle flow – An investigation on contact and cohesion models, *Procedia Eng.* 102 (2015) 1484–1490, <http://dx.doi.org/10.1016/j.proeng.2015.01.282>.
- [37] C. Bierwisch, T. Kraft, H. Riedel, M. Moseler, Three-dimensional discrete element models for the granular statics and dynamics of powders in cavity filling, *J. Mech. Phys. Solids* 57 (1) (2009) 10–31, <http://dx.doi.org/10.1016/j.jmps.2008.10.006>.
- [38] S. Radl, C.A. Radeke, J.G. Khinast, S. Sundaresan, Parcel-Based Approach for the Simulation of Gas-Particle Flows, 2011, URL <https://api.semanticscholar.org/CorpusID:172130652>.
- [39] D. Quetschiner, T. Lichtenegger, S. Pirker, S. Schneiderbauer, Multi-level coarse-grain model of the DEM, *Powder Technol.* 338 (2018) 614–624, <http://dx.doi.org/10.1016/j.powtec.2018.07.033>.
- [40] J. Tausendschön, J. Kolehmainen, S. Sundaresan, S. Radl, Coarse graining Euler-Lagrange simulations of cohesive particle fluidization, *Powder Technol.* 364 (2020) 167–182, <http://dx.doi.org/10.1016/j.powtec.2020.01.056>.
- [41] S. Heinrich, M. Dosta, S. Antonyuk, Multiscale analysis of a coating process in a Wurster fluidized bed apparatus, 46, 2015, pp. 83–135, <http://dx.doi.org/10.1016/bs.ache.2015.10.012>.
- [42] H. Che, H. Wang, L. Xu, R. Ge, Investigation of gas-solid heat and mass transfer in a Wurster coater using a scaled DEM-CFD model, *Powder Technol.* 406 (2022) 117598, <http://dx.doi.org/10.1016/j.powtec.2022.117598>.
- [43] H. Che, D. Liu, W. Tian, S. Gao, J. Sun, L. Xu, DEM-CFD study of gas-solid flow regimes in a Wurster type fluidized bed with experimental validation by electrical capacitance tomography, *Chem. Eng. J.* 389 (2020) 124280, <http://dx.doi.org/10.1016/j.ces.2020.124280>.
- [44] V. Brandt, J. Grabowski, N. Jurtz, M. Kraume, H. Kruggel-Emden, DEM and DEM-CFD modeling of systems with geometric constrictions using a new particle location based multi-level coarse graining approach, *Powder Technol.* (2024) 119447, <http://dx.doi.org/10.1016/j.powtec.2024.119447>.

- [45] C. Crowe, J. Schwarzkopf, M. Sommerfeld, Y. Tsuji, Continuous phase equations, in: *Multiphase Flows with Droplets and Particles*, second ed., CRC Press, 2011, <http://dx.doi.org/10.1201/b11103>.
- [46] T.-H. Shih, W.W. Liou, A. Shabbir, Z. Yang, J. Zhu, A new k- ϵ eddy viscosity model for high reynolds number turbulent flows, *Comput. & Fluids* 24 (3) (1995) 227–238, [http://dx.doi.org/10.1016/0045-7930\(94\)00032-T](http://dx.doi.org/10.1016/0045-7930(94)00032-T).
- [47] M. Askarishahi, M.-S. Salehi, S. Radl, Full-physics simulations of spray-particle interaction in a bubbling fluidized bed, *AIChE J.* 63 (7) (2017) 2569–2587, <http://dx.doi.org/10.1002/aic.15616>.
- [48] S. Madlmeir, T. Forgber, M. Trogrlic, D. Jajcevic, A. Kape, L. Contreras, A. Carmody, P. Liu, C. Davies, A. Sarkar, J. Khinast, Quantifying the coating yield by modeling heat and mass transfer in a Wurster fluidized bed coater, *Chem. Eng. Sci.* 252 (2022) 117505, <http://dx.doi.org/10.1016/j.ces.2022.117505>.
- [49] R. Sun, H. Xiao, Diffusion-based coarse graining in hybrid continuum–discrete solvers: Theoretical formulation and a priori tests, *Int. J. Multiph. Flow* 77 (2015) 142–157, <http://dx.doi.org/10.1016/j.ijmultiphaseflow.2015.08.014>.
- [50] J. Zhang, T. Li, H. Ström, B. Wang, T. Løvås, A novel coupling method for unresolved DEM-CFD modeling, *Int. J. Heat Mass Transfer* 203 (2023) 123817, <http://dx.doi.org/10.1016/j.jheatmasstransfer.2022.123817>.
- [51] R. Sun, H. Xiao, Diffusion-based coarse graining in hybrid continuum–discrete solvers: Applications in CFD–DEM, *Int. J. Multiph. Flow* 72 (2015) 233–247, <http://dx.doi.org/10.1016/j.ijmultiphaseflow.2015.02.014>.
- [52] C. Crowe, J. Schwarzkopf, M. Sommerfeld, Y. Tsuji, Particle-fluid interactions, in: *Multiphase Flows with Droplets and Particles*, second ed., CRC Press, 2011, <http://dx.doi.org/10.1201/b11103>.
- [53] D. Gunn, Transfer of heat or mass to particles in fixed and fluidised beds, *Int. J. Heat Mass Transfer* 21 (4) (1978) 467–476, [http://dx.doi.org/10.1016/0017-9310\(78\)90080-7](http://dx.doi.org/10.1016/0017-9310(78)90080-7).
- [54] H. Hertz, Ueber die Berührung fester elastischer Körper. 1882 (92), <http://dx.doi.org/10.1515/crll.1882.92.156>.
- [55] Y. Tsuji, T. Tanaka, T. Ishida, Lagrangian numerical simulation of plug flow of cohesionless particles in a horizontal pipe, *Powder Technol.* 71 (3) (1992) 239–250, [http://dx.doi.org/10.1016/0032-5910\(92\)88030-L](http://dx.doi.org/10.1016/0032-5910(92)88030-L).
- [56] M. Emam, L. Zhou, W. Shi, H. Chen, L. Bai, R. Agarwal, Theories and applications of CFD–DEM coupling approach for granular flow: A review, *Arch. Comput. Methods Eng.* 28 (2021) <http://dx.doi.org/10.1007/s11831-021-09568-9>.
- [57] T. Schwager, T. Pöschel, Coefficient of restitution and linear dashpot model revisited, *Granul. Matter* 9 (2007) <http://dx.doi.org/10.1007/s10035-007-0065-z>.
- [58] M. de Munck, E. Peters, J. Kuipers, Fluidized bed gas-solid heat transfer using a CFD-DEM coarse-graining technique, *Chem. Eng. Sci.* 280 (2023) 119048, <http://dx.doi.org/10.1016/j.ces.2023.119048>.
- [59] L. Lu, A. Morris, T. Li, S. Benyahia, Extension of a coarse grained particle method to simulate heat transfer in fluidized beds, *Int. J. Heat Mass Transfer* 111 (2017) 723–735, <http://dx.doi.org/10.1016/j.jheatmasstransfer.2017.04.040>.
- [60] M. Heine, S. Antonyuk, L. Fries, G. Niederreiter, S. Heinrich, S. Palzer, Modeling of the spray zone for particle wetting in a fluidized bed, *Chem. Ing. Tech.* 85 (3) (2013) 280–289, <http://dx.doi.org/10.1002/cite.201200148>.
- [61] S. Chialvo, J. Sun, S. Sundaresan, Bridging the rheology of granular flows in three regimes, *Phys. Rev. E* 85 (2012) 021305, <http://dx.doi.org/10.1103/PhysRevE.85.021305>.
- [62] D. Gidaspow, The fluidized state, in: *Multiphase Flow and Fluidization*, Academic Press, San Diego, 1994, pp. 97–114, <http://dx.doi.org/10.1016/B978-0-08-051226-6.50009-1>.
- [63] L. Lu, S. Benyahia, Method to estimate uncertainty associated with parcel size in coarse discrete particle simulation, *AIChE J.* 64 (7) (2018) 2340–2350, <http://dx.doi.org/10.1002/aic.16100>.
- [64] C. Windows-Yule, S. Benyahia, P. Toson, H. Che, A. Nicuşan, Numerical modelling and imaging of industrial-scale particulate systems: A review of contemporary challenges and solutions, *KONA Powder Part. J.* (2024) <http://dx.doi.org/10.14356/kona.2025007>.
- [65] A. Nikolopoulos, A. Stroh, M. Zeneli, F. Alobaid, N. Nikolopoulos, J. Ströhle, S. Karellas, B. Epple, P. Grammelis, Numerical investigation and comparison of coarse grain DEM-CFD and TFM in the case of a 1MWth fluidized bed carbonator simulation, *Chem. Eng. Sci.* 163 (2017) 189–205, <http://dx.doi.org/10.1016/j.ces.2017.01.052>.